Structural Models Constrained by Geophysical Data Provide Additional Insight to the Subsurface in Southern Colorado, U.S.A.*

M. Soledad Velasco[1], David Alumbaugh[1], Maggie Baber[1], and Joshua Poirier[1]

[1]NEOS GeoSolutions, Inc., Pleasanton, CA (solvelasco@yahoo.com)

Abstract

Onshore structurally complex areas combined with large amount of igneous intrusions can be difficult to image at depth with seismic data alone. The majority of the CO_2 fields of the northern Raton Basin of Southern Colorado are located in an area where seismic imaging is remarkably limited due to the mountainous terrain and the presence of high-velocity volcanic rocks which inhibit the resolution of the structural complexity at depth. We present a modeling/interpretation methodology that employs a combination of public domain gravity data with newly acquired ground magnetotelluric data and airborne magnetic and electromagnetic data, along with existing well and seismic data. The integration of these datasets are used to produce a series of 2D and 3D geophysical models that reveal basin architecture that is poorly defined through the limited seismic data alone. It also aids in decreasing uncertainty in the geologic cross-sections constructed and provides a better understanding of the structural complexities of the region. The structural interpretation from the gravity and magnetic data show two main sub-basins separated by a region of high density and magnetic susceptibility material that is likely related to igneous intrusions. This study also reveals two major structural styles: a SW-NE trend, believed to be related to the Proterozoic growth of the North American continent, and a younger NW-SE trend related to the Laramide orogeny with some reactivation of deep basement faulting. 3D EM inversion results reveal a robust basement architecture, outlining a conductive sedimentary basin overlying a resistive Precambrian basement. This multi-measurement acquisition and interpretation method demonstrates improvement of the overall understanding of the study area and may also aid in hydrocarbon exploration in regions where seismic exploration is challenging.

Introduction

NEOS GeoSolutions, Inc. undertook a multi-measurement, geological, and geophysical study in southern Colorado. The study area is geologically located on the northern edge of the Raton Basin, bound on the west by the Sangre de Cristo Mountains and on the east by the Wet Mountains and the Apishapa Arch (Figure 1). This basin is the southernmost Laramide foreland basin associated with the development of the ancestral Rocky Mountains. It is steeply dipping to overturned along the western flank and gently dipping on the eastern flank. During the

Laramide Orogeny in the Late Cretaceous through Early Tertiary, the Raton Basin deepened dramatically, resulting in a stratigraphic column of over 20,000 feet of Lower Paleozoic through Tertiary sedimentary rocks in the deepest part of the basin (Sims et al., 2001; Popov et al., 2001). From Late Oligocene to the present, the Sangre de Cristo Range was uplifted and the adjoining San Luis and Wet Mountain valleys were down-dropped by Rio Grande rifting (Lindsey et al., 1983). Rifting accompanied and followed intrusion of stocks, sills, and dikes of felsic and mafic igneous rock.

In this study, we present the interpretation of a combination of public domain gravity data with newly acquired ground magnetotelluric (MT) and airborne magnetic and electromagnetic (Z-Axis Tipper Electromagnetic or ZTEM) data (Lo and Zhang, 2008; Lo et al, 2009) (Figures 2A, 2B and 2C), along with existing well and seismic data. The integration of these datasets are used to produce a series of 2D and 3D geophysical models that reveal basin architecture over the entire region that cannot be obtained through the interpretation of the limited-availability seismic data alone.

Methodology and Results

NEOS acquired new geophysical data as well as downloading public domain data. In terms of potential field data, the gravity data employed are part of a publicly available dataset for the entire U.S. that is managed, and can be downloaded from the University of Texas, El Paso (UTEP). We downloaded these data and processed it in-house to produce the complete Bouguer corrected gravity map shown in Figure 2A. The magnetic data (Figure 2B) were collected concurrently with the airborne ZTEM data (Figure 2C) via helicopter in July and August of 2015. The helicopter acquisition resulted in a higher resolution magnetic data than publicly available. During the same time period, MT data were also acquired from 44 ground sites as shown in Figure 2C. Note that the number of sites as well as their locations was dictated by permitting issues and access constraints. Both electromagnetic datasets are of excellent quality, with the airborne ZTEM data spanning six frequencies over the range of 30 Hz to 720 Hz, and the MT data processed to provide frequency data between 0.001 Hz and 1 kHz.

All geophysical datasets were first analyzed independently and later used to create a 3D earth model. Both gravity and magnetic data were interpreted individually using various derivatives and filters to produce magnetic and gravity structural interpretation maps (Figures 2D and 2E). Although the public domain gravity data points are sparse, yielding a relatively low resolution grid, major structural features are still noticeable (Figure 2D). The gravity fault interpretation correlates very well with regionally mapped faults seen in the literature as well as with the interpretation of 2D seismic data. These data were also used for deep fault interpretation away from the seismic data. The structural interpretation from the gravity data show two main sub-basins separated by a region of high density material. The data also reveal the major NW-SE structural trend, and also suggest a perpendicular SW-NE trend that is separating these two sub-basins.

The high spatial resolution provided by the newly acquired magnetic data allowed us to clearly map faults and was invaluable for locating igneous intrusions, especially when interpreting from derivatives (Figure 2E). In these data, the main NW-SE trend is well recognized, and the perpendicular trend is strongly suggested. The two sub-basins are further defined, and the high density material area is confirmed with high magnetic susceptibility material, likely related to igneous intrusions. The magnetic data also helped in recognizing major dike orientations: radial, from large igneous intrusions; NW-SE, parallel to the major structural trend; SW-NE, perpendicular to major structural trend and parallel to interpreted suture zones at depth; and E-W, though a less common trend is also observed south of study area. The intrusions mapped

at the surface appear to continue at depth in most cases. The magnetic bodies mapped at depth and not observed at the surface are likely sources of the isolated shallow igneous bodies and swarms of dikes especially observed on the eastern part of the block, south of the Wet Mountains. The basement appears to be intruded by younger, higher susceptibility igneous rocks, not all of which are observed at the surface.

Interpretation of the 'raw' airborne ZTEM data was accomplished through maps of the Total Divergence, a processing technique that utilizes the in-line and off-line data and combines the two measurements into one image (Lo and Zhang, 2008). Similar to the magnetic and gravity data, the airborne ZTEM data also recognize the main NW-SE structural trend and, in addition, highly suggest the perpendicular SW-NE one, dividing the region in two sub-basins (Figure 2F). Figure 2C shows the 30 HZ in-phase data which represent the lowest frequency, and thus, deepest sensing component, of the acquired airborne ZTEM dataset. This image has the fault interpretation from the magnetic data overlain to show the excellent correlation between two complete separate datasets, corroborating the structural interpretation.

To determine a starting point for modeling of the various geophysical datasets, and to provide a basis for understanding the geologic structure and relationship between the sedimentary basin and the Precambrian basement, twelve 2D geologic cross-sections were built based on the combination of surface outcrops, seismic and well data, and constraints provided by the magnetic and gravity data. These 2D sections were chosen perpendicular to structure to best model the geology and based on key well locations and available public domain data. In areas where available, published cross-sections and seismic and well data interpretation were also used to better constrain the stratigraphy. An example section is shown in Figure 3A. In this profile, basement is represented by pink colors with a pattern fill, Paleozoic sediments by grays, Mesozoic by blues and greens, and Tertiary and Quaternary by beige.

Igneous intrusions are shown in gray with a fill pattern. Each geologic interval was given a density and susceptibility value, which were determined from measurement of field samples. If field samples were inaccessible, density values were determined via geophysical references and susceptibility values estimated using rock type knowledge and a susceptibility table from Applied Geophysics (Telford, Geldart, and Sheriff, 1990). The contact between the Precambrian basement and the sediments above denotes a large magnetic susceptibility contrast across the entire area, represented by long-wavelength, high-amplitude responses. Short-wavelength responses are also observed in the magnetic data, and these anomalies are interpreted to represent shallow intrusions of Tertiary age. Similarly, the gravity data suggest the highest density contrasts to be located across the boundary between the sedimentary basin and basement.

To increase the confidence of the potential field models, unconstrained joint electromagnetic (EM) inversions of the airborne ZTEM and MT data were run independently for each survey line using the workflow outlined in Alumbaugh et al. (in preparation). A total of 82 2D inversions were created, and Figure 3B is an example of these inversions, which corresponds to the same location as the potential field data and interpretation shown in Figure 3A. Analysis of these EM models indicates a general increase of resistivity with deepening of the geologic section, showing the lowest resistivity values within the Mesozoic sedimentary interval. The basement is observed with high resistivity values, as well as are most igneous intrusions.

Figure 3C shows the same resistivity model as in 3B with the interpretation of the geologic section in 3A, overlain. These two independent models show similar characteristics and indicate geological features that are in general agreement with one another. The basin is clearly outlined in the EM models, with a western boundary defined by a change in resistivity and represented in the potential field constrained

geologic models as a major basin bounding fault, which is also observed at the surface. In the case of Figure 3A, the intrusion at the surface in the center of the section is seen in the resistivity model as having higher resistivity than the surrounding sedimentary rocks. The lowest resistivity values (blue) are observed in the Mesozoic sedimentary package, possibly related to higher porosity rocks and/or the presence of thick low resistivity shale units in this section. The basement is emphasized with high resistivity (red), separating the sedimentary basin from the Precambrian basement.

As part of the basin architecture study, 3D modeling was performed using Geosoft's VOXI Earth Modeling software and service. The airborne magnetic data were used to generate a susceptibility model, and public-domain ground gravity data were used to generate a density model. Due to the non-unique nature of the inversion of magnetic data to recover spatial variability of susceptibility, constraints have been added to incorporate a priori geologic knowledge into the computation. For example, because the susceptibilities of all rocks within the survey area are expected to be greater than or equal to zero, a lower bound constraint of zero was incorporated to ensure positivity. The susceptibility modeling result is consistent with known geology and sheds light on the shape and location of intrusive bodies. Figure 4A shows the inverted result as a 3D volume.

Similar to the inversion of magnetic data described above, the inversion of gravity data to recover spatial variability of density in a 3D sense is very non-unique. In addition, sparse gravity data, as were used for this study, offer limited information on how density is varying with depth other than helping to resolve the larger scale basin and tectonic features. Thus, to make best use of the gravity data, a constrained inversion was performed that incorporated geological, geophysical, and petrophysical data as constraints to verify depth to basement across the area as well as determine if large scale density variations could be resolved within the sedimentary section and/or the basement. Upper and lower bounding constraints were utilized to help ensure consistency between the known geology and resulting distribution of density contrasts. Figure 4B shows a less dense basement to the west, which is also apparent in the 2D modeling and line data shown in Figure 3A. The main thrust fault is also clearly delineated trending NW-SE. The inversion also resolves lithology variation in the basement. This is most clear when comparing fitted basement densities west of the main thrust front to basement densities east of the front.

The last processing step in this analysis was combining the 82 2D joint inversions of the airborne ZTEM and MT data into a 3D resistivity volume. This was provided by first projecting each 2D resistivity solution into its true 3D position, and then using a geostatistical algorithm to interpolate between the lines onto a regular 3D grid shown in Figure 4C. The 3D resistivity model offers the best data to highlight basin features and the best estimate of basement depth as a sole measurement. This volume provides valuable information about basin geometry, including the lateral termination of Mesozoic younger clastics against thrust faults bounding the western side of the Raton Basin. The sedimentary basin boundary is well defined by a zone of low resistivity, especially the Mesozoic package highlighted in blue (Figure 4C). The western basin bounding fault is clearly highlighted by a resistivity contrast that correlates well with the main structural NW-SE trend. This EM model best reflects the 3D nature of this complex structural region.

Discussion

Regional crustal studies position the survey area within the transition zone of a complicated, bi-vergent subduction between two major provinces (Yavapai and Mazatzal) (Karlstrom and Humphreys, 1998). During the Precambrian, the NE-SW convergence between these major

provinces allowed for successive episodes of slab flattening and slab rollback, which led to shortening and rifting, respectively. These complex tectonic episodes are thought to have formed weak faults in the cratonic platform crust, which were then reactivated by stress transmitted during Phanerozoic compressional orogeny in the mid-continent (Marshak et al., 2000). Younger granitoids (approximately 1.72 Ga and younger) later intrude these accreted terrains and suture the North American continent along the accretionary shear zones (Amato et al., 2008). Sims et al. (2001) divide the basement in this region into blocks that are bound in NW-SE orientations consistent with Laramide structuring; however, they are interpreted as having variable movement through time due to changing stress fields.

During the Pennsylvanian, the ancestral Rocky Mountains existed as intra-cratonic block uplifts that formed as a result of the collision of the North America and South America-Africa plates. Deformation of the craton region during this time spread northwestward, and the Ancestral Rocky Mountains developed rapidly (Kluth and Coney, 1981). Inversion of basement-penetrating normal faults occurred during the Late Paleozoic Ancestral Rockies event and/or during the Mesozoic-Cenozoic Laramide event. It generated flat-topped uplifts bordered by outward-verging forced folds and faults with reverse-, oblique-, and strike-slip movements. These structures, divided into two sets on the basis of orientation (northeast and northwest), formed by inversion of Proterozoic extensional-fault systems (Cooper and Williams, 1989; Marshak et al., 2000).

The structural interpretation derived from all geophysical datasets show two main sub-basins separated by a region of high density and high susceptibility material, likely related to intrusions. This region, at the surface, is composed of a NE-SW trending succession of igneous intrusions all aligned in this orientation. The data also reveal the major NW-SE structural trend, however, they also suggest a perpendicular SW-NE trend that is separating these two sub-basins. This trend is likely related to planes of weakness associated with the Precambrian suture zones mentioned above. It is possible that the structural blocks may have had multiple episodes of tectonic stress and thus, multiple periods of differential up and down movement. Faulting, in this region, appears to be both related to the Proterozoic accretionary model of North America (SW-NE shear zones), as well as NW-SE faulting believed to have been rejuvenated during the Laramide Orogeny.

The results from the inversion of EM data also reveal a potential less resistive layer beneath a resistive, and outcropping, basement along the westernmost thrust fault that forms the Sangre de Cristo Mountains. This contrast might be suggesting the location of a low-dipping fault that would place the Precambrian basement overthrusting a sedimentary package, likely Paleozoic in age. This is interpretation is in agreement with previous work done by Lindsey et al. (1986), and Ruleman and Machette (2007). If this is the case, it enhances the hydrocarbon play potential existing in this region.

Conclusions

The combination of all available datasets was successful at creating an integrated earth model with an ultimate outcome of increasing the information available for the study area. New interpreted dikes and faults not visible at the surface were added to this integrated model. This multi-measurement method was successfully able to recognize the main NW-SE structural trend of the basin and another perpendicular trend (SW-NE), not clearly visible at the surface, likely related to planes of weakness associated with Precambrian suture zones. This integrated methodology was also able to identify two sub-basins separated by a structural high related to igneous emplacements, as well as isolate the

location of igneous intrusions and dikes, and their associated magnetic source bodies at depth. This method also allowed the mapping of the Precambrian basement and its relationship with the overlaying sedimentary basin.

References Cited

Alumbaugh, D., H. Huang, J. Livermore, and M.S. Velasco, 2016, Resistivity imaging in a fold and thrust belt using ZTEM and sparse MT data, in preparation for publication in *First Break*.

Amato, J.M., A.O. Boullion, A.M. Serna, A.E. Sanders, G.L. Farmer, and G.E. Gehrels, 2008, Evolution of the Mazatzal province and the timing of the Mazatzal orogeny: Insights from U-Pb geochronology and geochemistry of igneous and metasedimentary rocks in southern New Mexico: Geological Society of America Bulletin, v. 120/3-4, p. 328-346.

Cooper, M.A., and G.D. Williams, 1989, Inversion tectonics: Geological Society London Special Publication 44, 375 p.

Karlstrom, K.E., and E.D. Humphreys, 1998, Persistent influence of Proterozoic accretionary boundaries in the tectonic evolution of southwestern North America: Interaction of cratonic grain and mantle modification events: Rocky Mountain Geology, v. 33, p. 161-180.

Kluth, C.F., and P.J. Coney, 1981, Plate tectonics of the Ancestral Rocky Mountains: Geology, v. 9, p. 10-15.

Lindsey, D.A., B.J. Johnson, and P.A.M. Andriessen, 1983, Laramide and Neogene structure of the Sangre de Cristo Range, south-central Colorado, *in* J.D. Lowell, ed., Rocky Mountain foreland basins and uplifts: Rocky Mountain Association of Geologists, p. 219-228.

Lindsey, D.A., B.R. Johnson, S.J. Soulliere, R.M. Bruce, and K. Hafner, 1986, Geologic map of the Beck Mountain, Crestone Peak, and Crestone quadrangles, Custer, Huerfano, and Saguache counties, Colorado: U.S. Geological Survey Miscellaneous Field Studies Map MF-1878, scale 1:24,000.

Lo, B., and M. Zhang, 2008, Numerical modeling of Z-TEM (airborne AFMAG) responses to guide exploration strategies: SEG Technical Program Expanded Abstracts, p. 1098-1102.

Lo, B., J.M. Legault, P. Kuzmin, and M. Combrink, 2009, ZTEM (airborne AFMAG) tests over unconformity uranium deposits: 20th Australian Society of Exploration Geophysicists International Conference and Exhibition, Extended Abstracts, 4 p.

Marshak, S., K. Karlstrom, and J. Timmons, 2000, Inversion of Proterozoic extensional faults: An explanation for the pattern of Laramide and Ancestral Rockies intracratonic deformation, United States: Geology, v. 28, p. 735-738.

Popov, M., V. Nuccio, T. Dyman, T. Gognat, R. Johnson, J. Schmoker, M. Wilson, and C. Bartberger, 2001, Basin-centered gas systems of the U.S.: USGS open-file report 01-135, version 1.0

Ruleman, C., and M. Machette, 2007, An overview of the Sangre de Cristo Fault System and new insights to interactions between Quaternary faults in the Northern Rio Grande Rift: USGS open file 07-1193, Ch. J.

Sims, P., V. Bankey, and C. Finn, 2001, Preliminary Precambrian basement map of Colorado, a geological interpretation of the Aeromagnetic anomaly map: USGS Open-File Report 01-364.

Telford, W.M., L.P. Geldart, and R.E. Sheriff, 1990, Applied Geophysics (2nd ed.), New York, New York: Cambridge University Press.
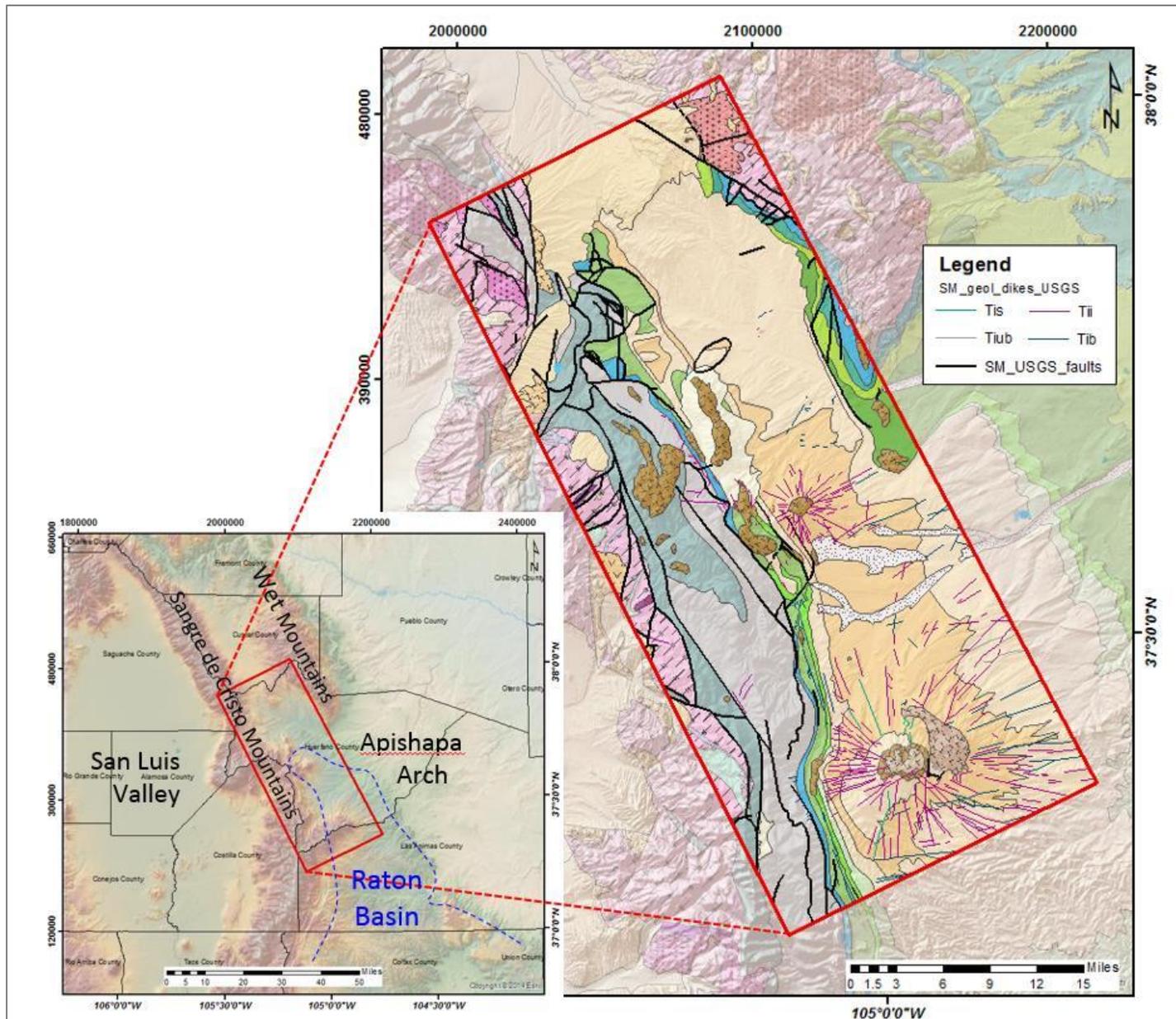
Figure 1. Geologic map of the study area (inset map shows the location of the study area). Note the pronounced NW-SE structural trend (faults represented in black solid lines) and extensive volcanism and intrusions (brown polygons) (colored solid lines are dikes).
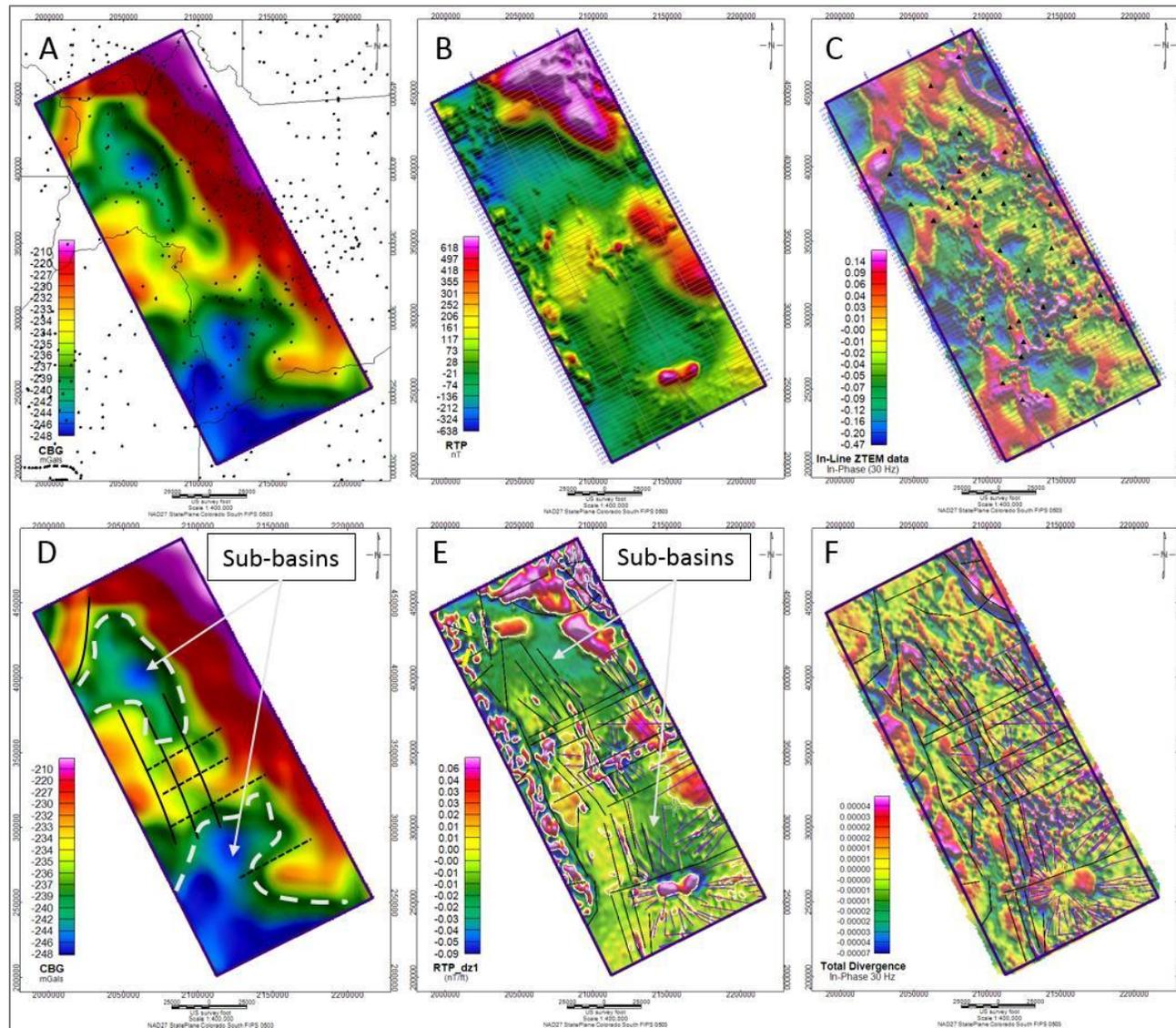
Figure 2. (A) Map showing Complete Bouguer Gravity (CBG) with ground stations shown in black dots. (B) Map showing the Reduced-To-Pole (RTP) magnetic data with survey outline in gray solid lines. (C) Map showing the in-line component of the airborne in-phase 30 Hz ZTEM data with survey outline in gray lines and ground MT sites represented by black triangles. (D) Map showing the interpretation of the CBG data (background). (E)Map showing the first vertical derivative (dz1) of the RTP data with interpretation of faults (black lines), volcanic dikes (violet lines), and magnetic bodies outline (white polygons). (F) Map showing total divergence of the in-phase 30 Hz airborne ZTEM data with structural and dikes interpretation derived from magnetic data overlain for comparison. Note the good correlation between datasets outlining the two major structural trends observed (NW-SE and NE-SW).
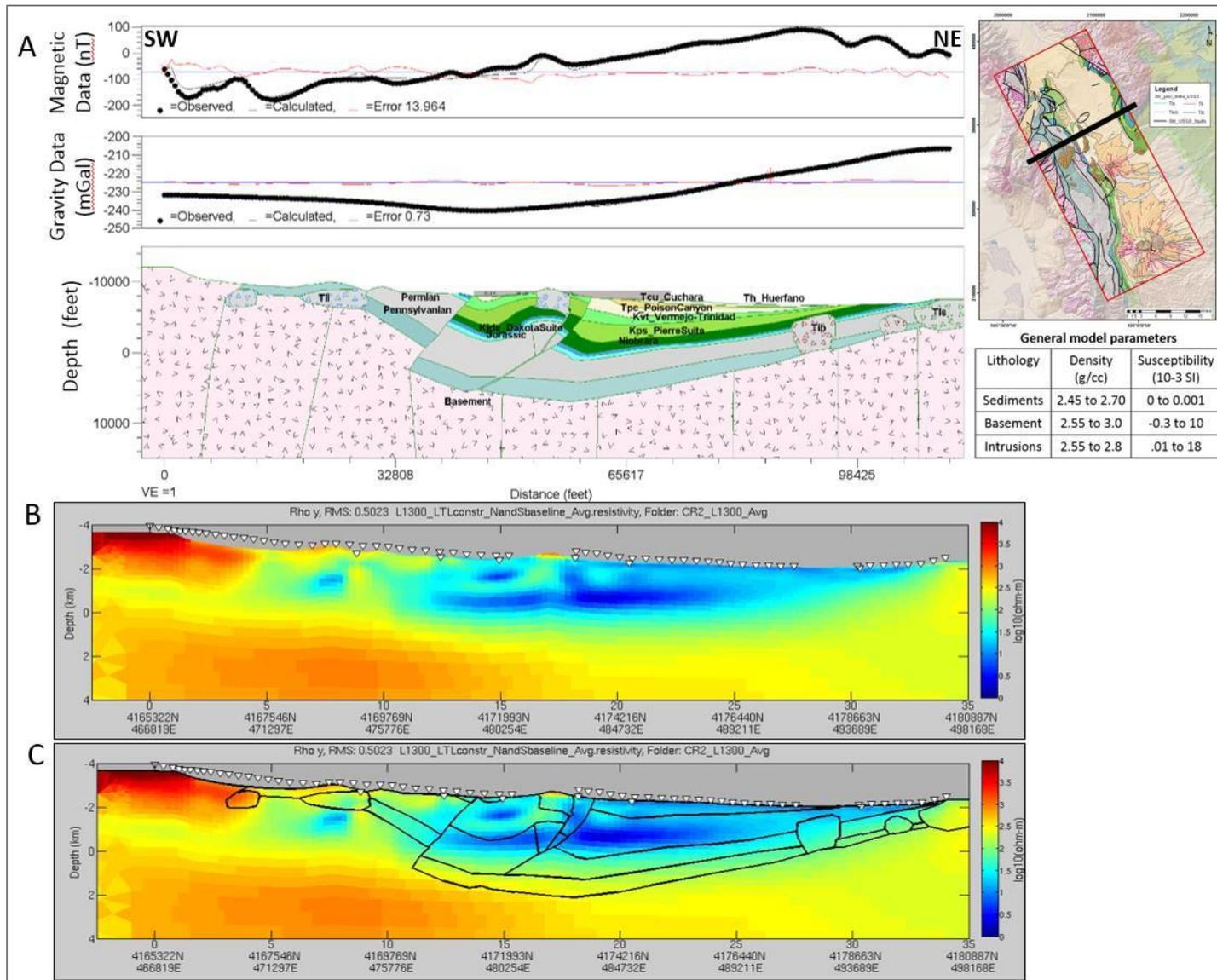
Figure 3. (A) Example of the 2D profiles. Black circles in the magnetic and gravity panels above the section represent the input magnetic and gravity data, respectively. Black lines in the top two panels represent the values calculated from the models; the red line represents the difference or error between the measured data and calculated results. Top right corner shows map with profile location. Model parameters are immediately below. (B) Resistivity image product of the joint inversion of the airborne EM and ground MT data. Same resistivity image from B with interpretation overlain from section in A, above.
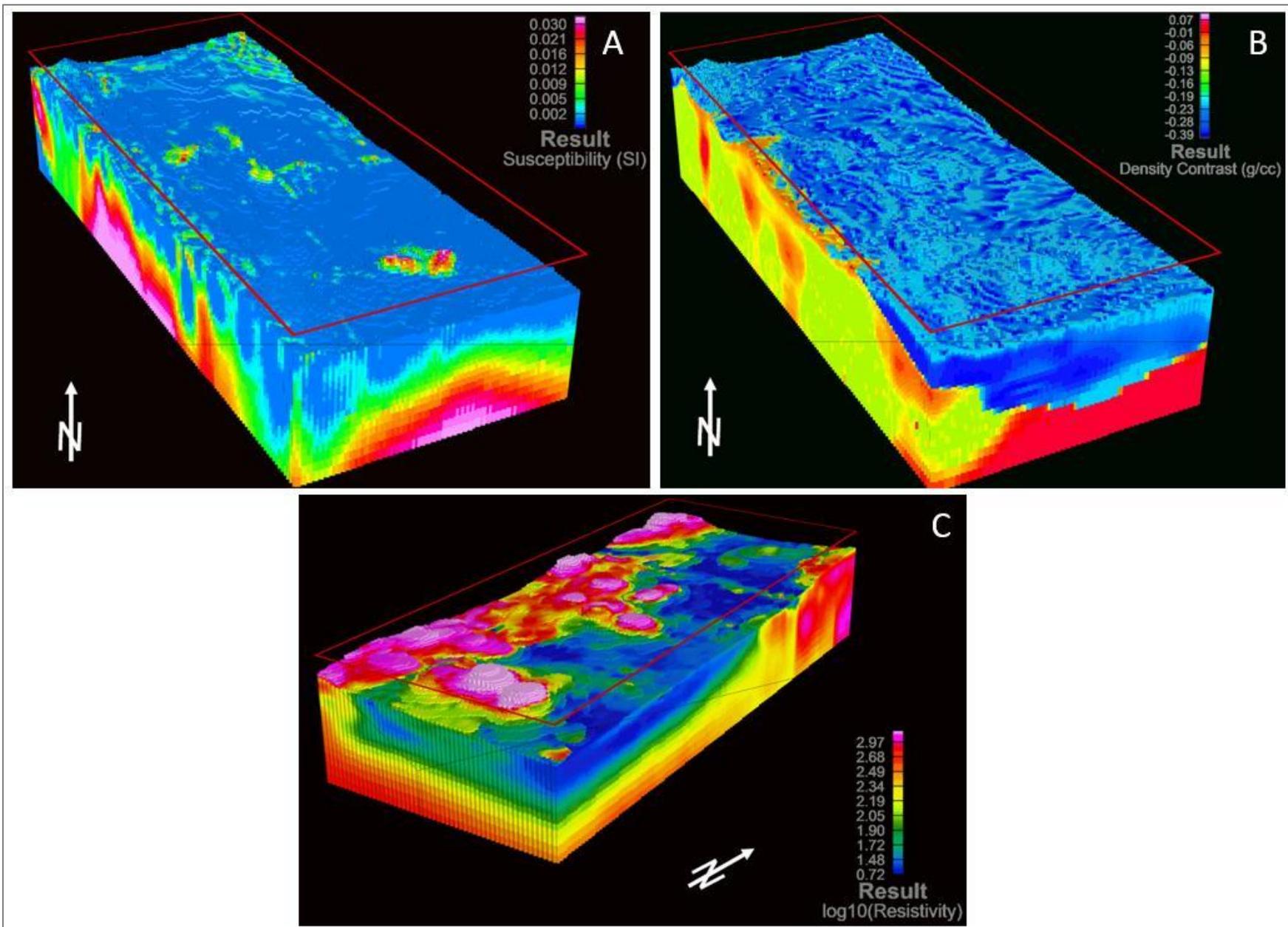
Figure 4. (A) 3D density volume resulting from the constrained inversion of the gravity data, (B) 3D magnetic susceptibility volume resulting from the inversion of the residual magnetic intensity data, and (C) 3D resistivity volume resulting from the merging of 2D joint inversions of the airborne EM and MT data.